Materials Science & Engineering A 803 (2021) 140498

Contents lists available at ScienceDirect

Materials Science & Engineering A

journal homepage: http://www.elsevier.com/locate/msea

Ultra-high tensile strength via precipitates and enhanced martensite transformation in a FeNiAlC alloy

Yan Ma [a,b], Lingling Zhou [a], Muxin Yang [a], Fuping Yuan [a,b,*], Xiaolei Wu [a,b]

[a] State Key Laboratory of Nonlinear Mechanics, Institute of Mechanics, Chinese Academy of Sciences, No. 15 West Road, North 4th Ring, Beijing, 100190, China
[b] School of Engineering Science, University of Chinese Academy of Sciences, No. 19(A) Yuquan Road, Beijing, 100049, China

ARTICLE INFO

Keywords:
Strain hardening
Transformation-induced plasticity
Heterogeneous structures
Precipitates
Twins

ABSTRACT

Aging and quenching at critical temperatures were applied to a hot-rolled (HR) Fe-24.86Ni-5.8Al-0.38C (mass%) dual-phase alloy to obtain B2 precipitates with various volume fractions and sizes. Higher yield strength and stronger strain hardening were achieved in the aged samples compared to these for the HR sample, and the corresponding deformation mechanisms were carefully revealed. The aged samples show stronger hetero-deformation induced hardening compared to that for the HR sample. The amount of phase transformation during tensile tests is much higher for the aged sample compared to that for the HR sample due to the reduced stability of the austenite phase, which can be attributed to the high local stress level induced by undeformable and hard B2 precipitates around the austenite grains and reduction of nickel and aluminum in the austenite phase by diffusion from the austenite phase to the B2 precipitates during aging. Deformation-induced lath martensite with high dislocation density can be observed after tensile deformation, and these transformation-induced dislocations should have great impact on the strain hardening. Moreover, the density of twins becomes much higher for the martensite grains after tensile deformation, and these deformation-induced nanotwins should contribute significantly to the strain hardening, as the dynamic Hall-Petch effect.

1. Introduction

High strength in metals and alloys has always been desirable for structural applications [1,2]. However, high strength generally is accompanied by a low rate of strain hardening and limited ductility [3,4]. In the past decades, several strategies have been developed to achieve both high strength and good ductility in metals and alloys, such as twinning-induced plasticity (TWIP) steels [5,6], transformation-induced plasticity (TRIP) steels [7,8], nanotwinned metals [9,10], heterogeneous gradient [11,12]/multimodal [13–15]/lamella structures [16–19], nano-precipitates [20,21]. Among them, TWIP and TRIP steels have been widely used in the automobile industries, in which the yield strength, the ultimate strength and the strain hardening ability are the most important parameters of design for light weight and safety improvement [5,7]. While these parameters are mutually exclusive in general, i.e., higher yield strength usually results in lower strain hardening [22,23].

In the metals and alloys with TRIP effect, the strain hardening and the ductility can be much enhanced by the displacive phase transformation upon plastic deformation [24,25]. The stress/strain partitioning between the pre-existing phases and the new produced hard phase can build the back stress hardening and the accumulation of geometrically necessary dislocations (GNDs) at the phase interfaces [26,27]. The deformation-induced transformation behaviors are generally influenced by the thermodynamic stability of the austenite phase, which in turn is directly related to the initial grain size of the austenite phase, the initial phase fractions, elemental partitioning and the stress/strain partitioning between different phases during the tensile deformation [25–27]. Previous studies have shown that simultaneous improvement of yield strength and strain hardening could be achieved by varying grain sizes and initial phase fractions [25,28,29].

The deformation-induced transformation behaviors and deformation twins were generally found to be related to the stress levels around the austenite grains, which could be regulated by temperature and strain rate [30–32]. Moreover, deformation twins and TRIP effect can also be enhanced through raising the local stress levels by introducing intermetallic precipitates around the austenite grains [33–36], resulting in stronger strain hardening and better tensile ductility. In this regard, aging and quenching at critical temperatures were applied to a hot-rolled (HR) FeNiAlC alloy to obtain B2 intermetallic precipitates

* Corresponding author. Institute of Mechanics, Chinese Academy of Sciences, No. 15 West Road, North 4th Ring, Beijing, 100190, China.
E-mail address: fpyuan@lnm.imech.ac.cn (F. Yuan).

https://doi.org/10.1016/j.msea.2020.140498
Received 21 September 2020; Received in revised form 5 November 2020; Accepted 6 November 2020
Available online 9 November 2020

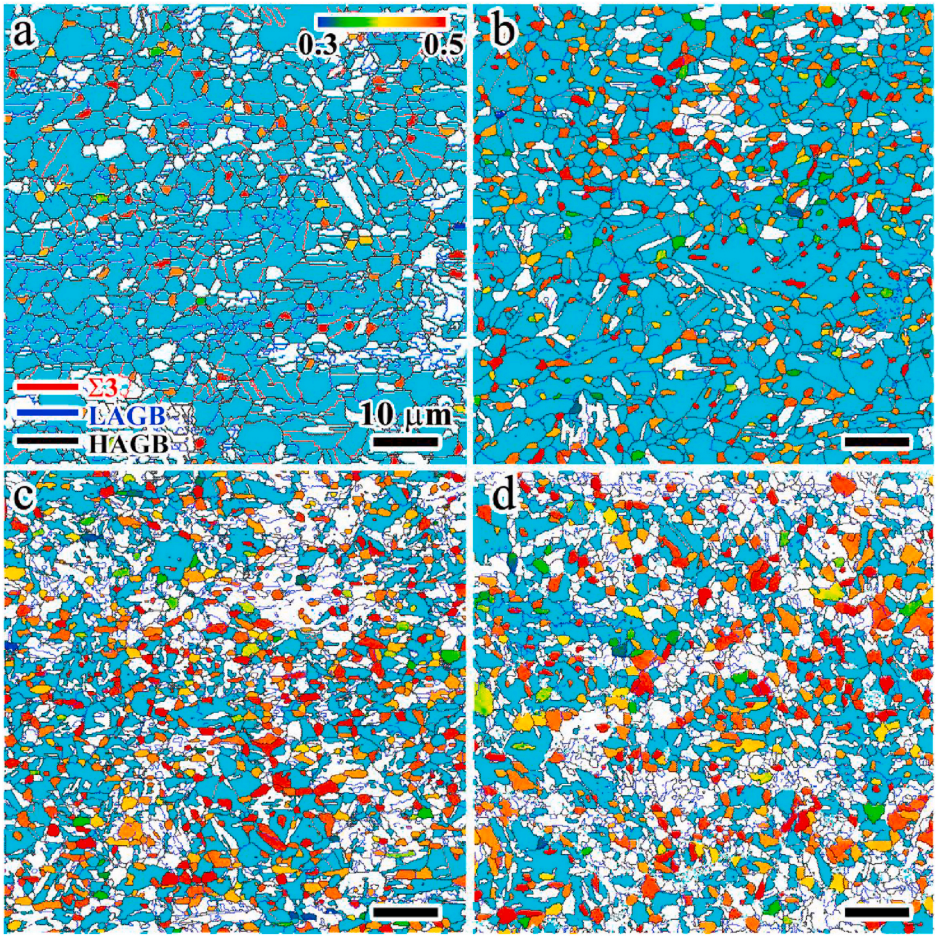

Fig. 1. EBSD phase images with GBs of initial microstructures: (a) for the HR sample; (b) for the aged sample at 550 °C; (c) for the aged sample at 650 °C; (d) for the aged sample at 750 °C.

with various volume fractions and various sizes for achieving larger yield strength and stronger strain hardening. The corresponding deformation mechanisms for this FeNiAlC alloy reinforced with B2 intermetallic precipitates were carefully revealed by load-unload-reload (LUR) tests, X-ray diffraction (XRD) measurements, electron backscattered diffraction (EBSD), and transmission electron microscopy (TEM).

2. Materials and experimental procedures

The Fe-24.86Ni-5.8Al-0.38C (mass%) alloys were prepared by arc-melting pure elements in an argon atmosphere and subsequently cast into an iron mold. The mechanical properties for this alloy with severe plastic deformation condition have been investigated previously [37–39]. The as-cast ingots were first hot-forged at 950 °C with the final dimensions of 10 × 10 × 50 mm^3. Then the resulting plates were solution-treated at 1100 °C for 4 h and followed by hot-rolling (HR) with a total thickness reduction of ~60% at 950 °C. The final sheets were aged at 550 °C, 650 °C and 750 °C for 1 h (marked as 550, 650, and 750). The sheet without aging treatment was marked as HR. All heat treatments were finished by water quenching (WQ).

The mechanical properties were evaluated by tensile testing using MTS 793 machine at an engineering strain rate of 5 × 10^{-4} s^{-1}. Dog-bone-shaped tensile specimens were fabricated by electro-discharge machining with a gauge section of 4 × 1 mm^2 and 15 mm in length. In order to verify reproducibility of the data, more than three tensile specimens were tested for each sample. Load-unload-reload (LUR) tests were performed to investigate the back stress hardening and the back stress was obtained by the method in the previous research [40,41].

Volume fractions of various phases were estimated by XRD (Rigaku Smart Lab 9) with Cu K_α radiation (λ = 1.5406 Å) at 35 kV. The Ni-K_β filter was used to absorb most K_β X-rays for more accurate diffractogram analysis. The volume fraction of austenite phase, V_γ, was calculated using the equation, $V_\gamma = \frac{1.4I_\gamma}{1.4I_\gamma + I_\alpha}$, where I_γ and I_α are the direct integrated intensities of the $(220)_\gamma$, $(311)_\gamma$, and $(211)_\alpha$ diffraction peaks in the 2θ−range [42]. Microstructure characterizations were carried out using SEM (JEOL JSM-7001F) and TEM (JEOL JEM-2100F). The TEM thin foils were cut from the gauge sections of the tensile specimens, mechanically thinned to a thickness of ~50 μm, and finally etched by a twin-jet electro-polishing using a solution of 5% perchloric acid and 95% ethanol at −25 °C. EBSD characterizations were analyzed using the TSL OIM data-collection software. The EBSD images were used to distinguish the B2 precipitates from the BCC phase (α' martensite). The Schmid factor of B2 intermetallic precipitates was calculated with the BCC slip systems of $\{1\bar{1}0\}\langle 111\rangle$, and the applied load direction parallel to the horizontal line of the plane. The kernel average misorientation (KAM) values were calculated to evaluate the intragranular dislocation density. The grain boundaries (GBs) with the misorientation angle larger than 15° were defined as high angle grain boundaries (HAGBs), and GBs with the misorientation angle between 5 and 15° were defined as low angle grain boundaries (LAGBs). The other details about the microstructure characterization, the X-ray diffraction (XRD) measurements and the mechanical tests can be found in our recent work [37].

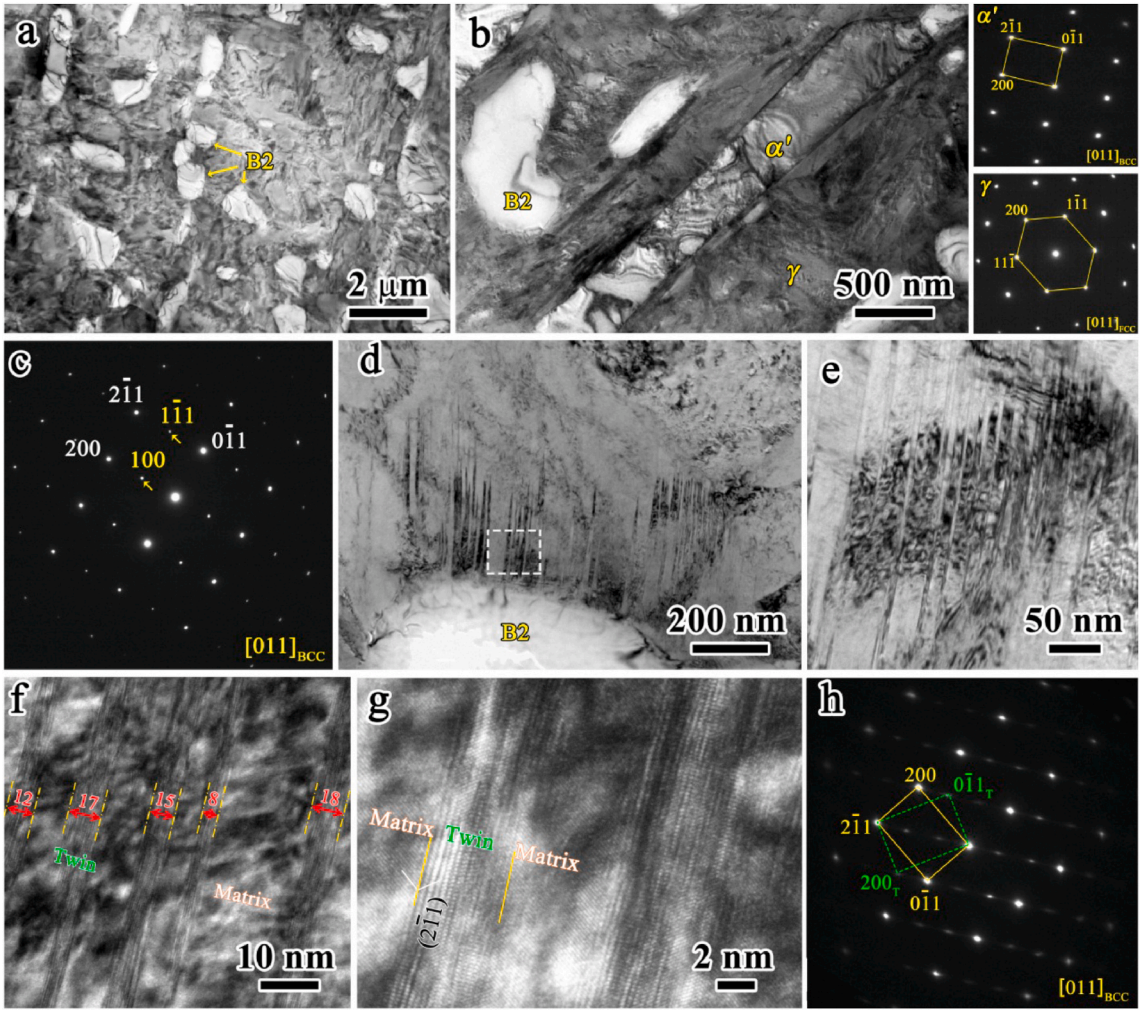

Fig. 2. TEM images of initial microstructures for the sample aged at 550 °C. (a) The shape, size and distribution of the B2 precipitates. (b) A close-up view of bright-field TEM image showing austenite, martensite and B2 grains. (c) SAD pattern showing superlattice structure for B2 precipitates. (d) A martensite grain with high density of twins adjacent to a B2 precipitate. (e) The close-up view for the rectangle area in (d). (f) and (g) High resolution TEM images showing the details of twins in the martensite phase. (h) SAD pattern showing the twin relationship in the martensite grains.

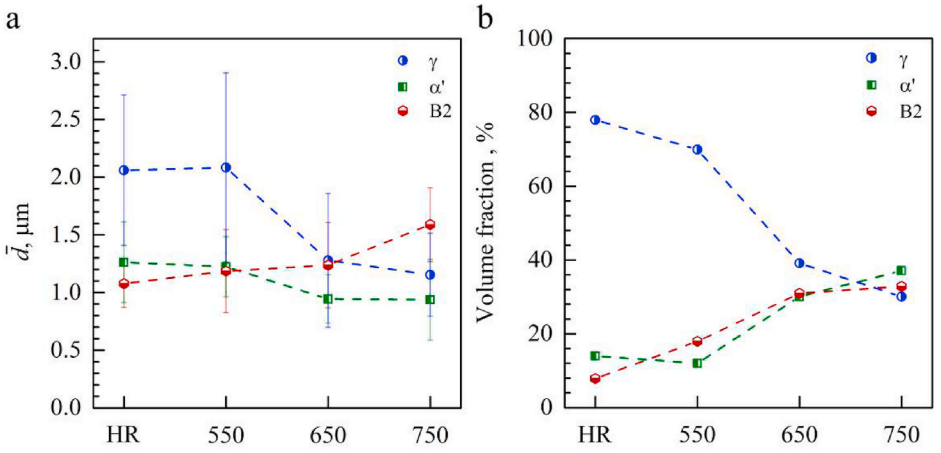

Fig. 3. (a) The estimated average grain sizes of austenite grains, martensite grains and B2 precipitates for various samples. (b) The volume fractions of austenite phase, martensite phase and B2 precipitate for various samples.

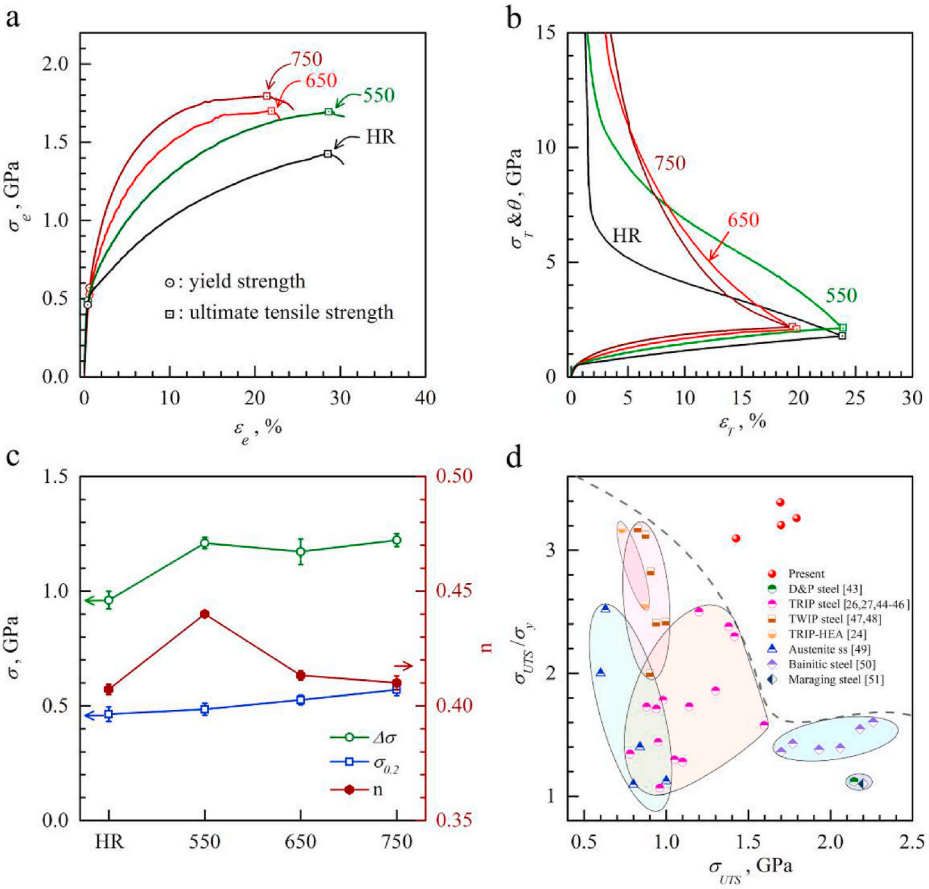

Fig. 4. The tensile properties for various samples. (a) The engineering stress-strain curves for various samples. (b) The true stress and hardening rate (θ) as a function of true strain for various samples. (c) The yield strength, the strain hardening exponent (n) and $\Delta\sigma$ for various samples. (d) The ratio between the ultimate strength and the yield strength as a function of the ultimate strength for the data from the present samples, along with the data from the other engineering metals and alloys.

3. Results and discussions

The initial microstructures prior to tensile loading for various samples are shown in Figs. 1 and 2. The EBSD phase images with grain boundaries (GBs) for various samples are displayed in Fig. 1a–d. In Fig. 1a–d, $\sum 3$ twin boundaries (TBs), LAGBs and HAGBs are displayed with red, blue and black lines. The austenite (γ phase) grains and the martensite (α' phase) grains are indicated by light green and white colors, while the B2 intermetallic precipitates are colored based on the magnitude of Schmid factor (the scale bar is shown in Fig. 1a) in Fig. 1a–d. As indicated, all samples show a dual-phase microstructure reinforced by B2 intermetallic precipitates, hereon referred as "triplex microstructure". In the HR sample, lots of LAGBs can be observed and most of these LAGBs are found to turn into HAGBs after aging and WQ. Numerous $\sum 3$ TBs can also be observed in the austenite grains of the HR sample, and the density of $\sum 3$ TBs is observed to decrease with increasing aging temperature in the aged and WQ samples. In all samples, the magnitude of Schmid factor of B2 intermetallic precipitates is close to 0.5, which indicates that these B2 intermetallic precipitates with high Schmid factors are hard and nearly undeformable.

The TEM images for the typical aged sample at 550 °C are shown in Fig. 2. The shape, size and distribution of the B2 intermetallic precipitates are shown in the bright-field TEM image of Fig. 2a, in which the precipitates show brighter diffracting contrast. As indicated, the size of precipitates is at 1–2 μm or submicron level, and these precipitates are observed to distribute evenly among the austenite matrix. A close-up view of bright-field TEM image showing austenite, martensite and B2 grains is given in Fig. 2b, in which the insets of selected area diffraction (SAD) identify the γ phase and the α' phase. While, the SAD showing the B2 precipitates is displayed in Fig. 2c. The B2 phase can be confirmed by the $(001)_{B2}$ superlattice reflection seen in the [011] B2 zone axis microdiffraction pattern (Fig. 2c). Previous study [33] has shown that Ni and Al elements are segregated in the B2 precipitates. Lath martensite and B2 particles are observed to nucleate inside the austenite grains. Lots of twins are also observed in the martensite grains, as shown in Fig. 2d and the corresponding close-up view in Fig. 2e. These twins are formed due to the high local stress induced by the volume expansion during the WQ-induced martensite transformation. The high-resolution TEM images showing the details of twins are displayed in Fig. 2f and g. These twins are found to have about 10 atom-layer thickness, and the twin plane is identified as $(2\bar{1}1)$. The TEM images were recorded by orienting the martensite grains close to their [011] zone axis, so that the twins of martensite grains are easy to identified (the SAD showing the twin relationship in the martensite grains is given in Fig. 2h). The high density of twins in martensite grains with nanoscale size should have strong influence on the strengthening and strain hardening for the microstructures.

The estimated average grain sizes of austenite grains, martensite grains and B2 precipitates for the HR sample and the aged samples are shown in Fig. 3a, while the volume fractions for these three phases for various samples are displayed in Fig. 3b. It is shown that the average grain size of austenite grains for the aged sample at 550 °C is slightly larger than that for the HR sample, which is due to the grain coarsening of recovery during annealing since there is no obvious phase transformation from austenite phase to martensite phase during WQ. While, the average grain sizes of austenite grains for the aged samples at 650 and 750 °C are observed to become much smaller compared to that for the HR sample, which is due to the significant phase transformation

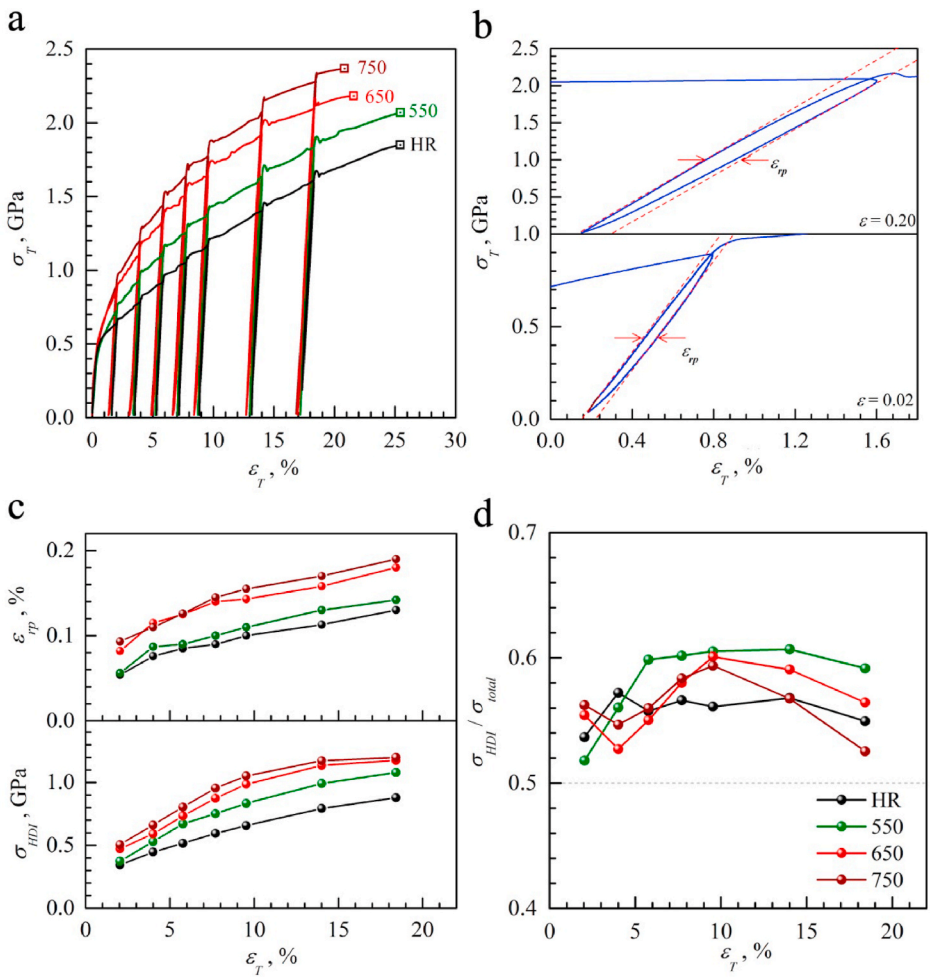

Fig. 5. HDI hardening for various samples. (a) The true stress-strain curves for LUR tests. (b) The close-up views of typical hysteresis loops for the aged sample at 750 °C. (c) Both σ_{HDI} and ε_{rp} as a function of applied true tensile strain for various samples. (d) The evolutions of $\sigma_{HDI}/\sigma_{total}$ along with true applied tensile strain for various samples.

from austenite phase to martensite phase during WQ and the nucleation of martensite grains inside the austenite grains. The transformed martensite grains during WQ are lath like, and the width of formed lath martensite grains is very small. Thus, the average grain sizes of martensite grains for all aged samples are smaller than that for the HR sample, and decrease with increasing aging temperature due to the increased volume fraction of the small size lath martensite during WQ. The average grain size and the volume fraction of the B2 precipitates for all aged samples are found to be larger than those for the HR sample, and both increase with increasing aging temperature. The volume fraction of martensite phase for the aged sample at 550 °C is almost the same as that for the HR sample since there is no obvious martensite transformation during WQ at this temperature, while the volume fraction of martensite phase increases significantly at larger aging temperature due to the obvious martensite transformation during WQ. The volume fraction of the austenite phase was observed to be much reduced for the aged samples and decrease with increasing aging temperature, which is due to the martensite transformation during WQ and the formation of B2 precipitates inside the austenite grains during aging.

The tensile properties for various samples are shown in Fig. 4. The engineering stress-strain curves are displayed in Fig. 4a, in which the yield points and the ultimate strength (UTS) points are marked by circles and squares, respectively. It is interesting to note that both the yield strength and the strain hardening ability (the difference between the UTS and the yield strength, $\Delta\sigma = \sigma_{UTS} - \sigma_y$, can be considered as an indicator of the strain hardening ability) were observed to be elevated after aging and WQ treatment compared to those for the HR sample. Especially for the sample aged at 550 °C, yield strength and ultimate tensile strength are simultaneously improved without sacrificing tensile ductility compared to those for the HR sample. The true stress and hardening rate (θ) are plotted as a function of true strain for various samples in Fig. 4b. It is indicated that the strain hardening rate is much enhanced after aging and WQ treatment, and the aged sample at 550 °C shows the highest hardening rate. The well-known Ludwik's equation, $\sigma = \sigma_0 + K\varepsilon^n$ (where σ_0 is the yield stress, K is the strength coefficient, n is the strain hardening exponent) can be used to fit the true stress-strain curves for our samples to obtain the strain hardening exponent, which is another indicator of strain hardening ability. Thus, the yield strength, the strain hardening exponent and $\Delta\sigma$ are plotted as a function of aging temperature in Fig. 4c. As indicated in Fig. 4c, the yield strength and $\Delta\sigma$ are both improved after aging and WQ treatment, and they both increase with increasing aging temperature. It also can be seen that the strain hardening exponent (n) is improved after aging and WQ treatment, and the aged sample at 550 °C has the highest n. Moreover, the ratio between the ultimate strength and the yield strength is plotted as a function of the ultimate strength for the data from the present samples in Fig. 4d, along with the data from the other engineering metals and alloys, such as D&P steel [43], TRIP steel [26,27,44–46], TWIP steel [47,48], TRIP-high entropy alloy [24], austenite stainless steel [49], bainitic steel [50] and maraging steel [51]. This plot indicates that the present alloy with triplex microstructures has superior strain hardening ability along with high ultimate tensile strength, and the corresponding deformation

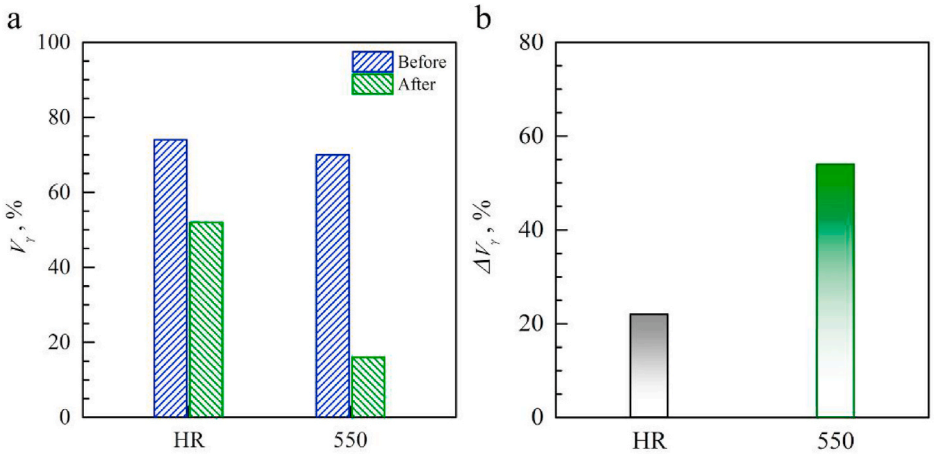

Fig. 6. (a) The volume fractions of γ austenite phase prior to and after tensile deformation. (b) The amounts of phase transformation during tensile tests.

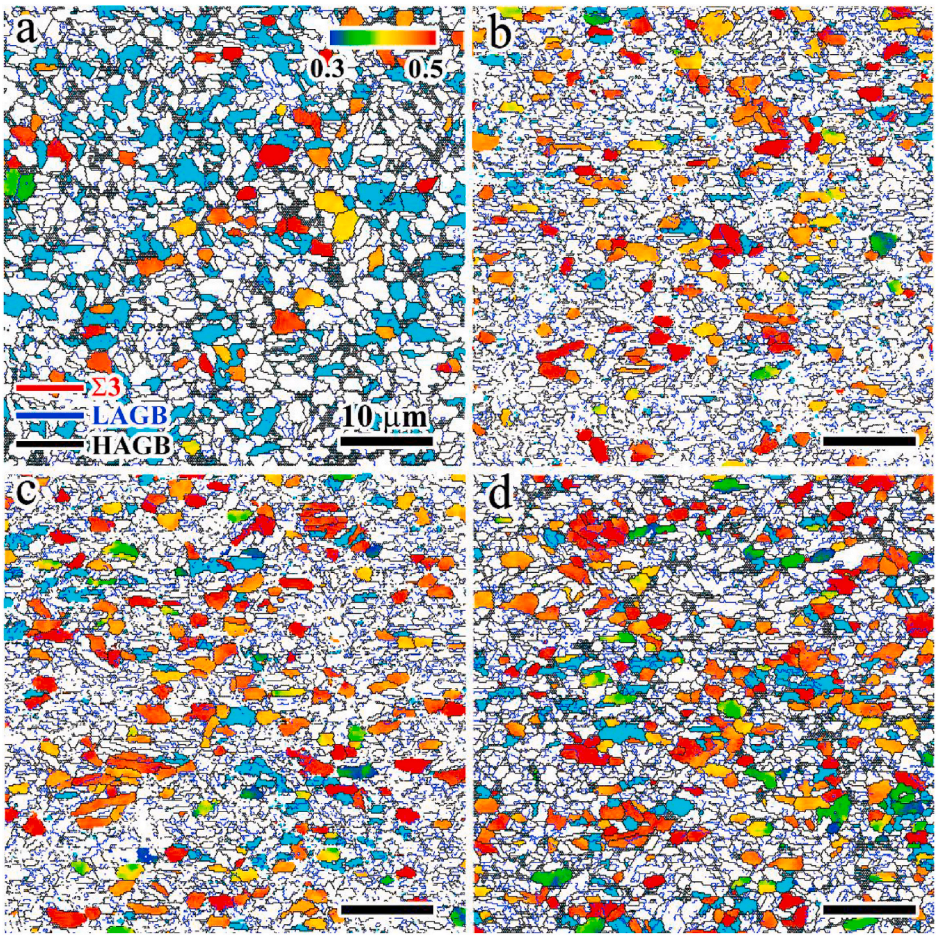

Fig. 7. EBSD phase images with GBs after tensile deformation: (a) for the HR sample; (b) for the aged sample at 550 °C; (c) for the aged sample at 650 °C; (d) for the aged sample at 750 °C.

mechanisms will be revealed next by LUR tests and microstructure characterizations.

As indicated in previous studies [37,40,41], the high strain hardening in metal and alloys with dual-phase microstructure can be attributed to the back stresses arising from the plastic deformation incompatibility between the different phases, and the back stress hardening can be even more significant when the martensite transformation occurs during the tensile deformation. In a recent review [52], the extra hardening in heterogeneous materials is proposed to be resulted from interactions between back stresses developed in soft domains and forward stresses developed in hard domains, and should be described as hetero-deformation induced (HDI) hardening. In this regard, the HDI stresses for various samples were characterized by LUR tests, and the true stress-strain curves for LUR tests are shown in Fig. 5a. It is interesting to note the obvious yield-drop phenomenon emerged from the new yield stress upon each reloading in LUR tests for all samples. This

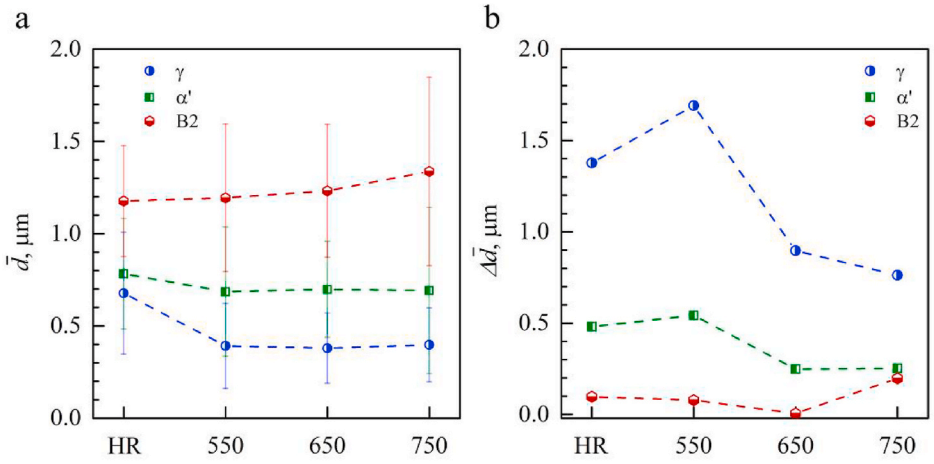

Fig. 8. (a) The estimated average grain sizes of austenite grains, martensite grains and B2 precipitates after tensile testing for various samples. (b) The average size reductions of austenite grains, martensite grains and B2 precipitates after tensile testing for various samples.

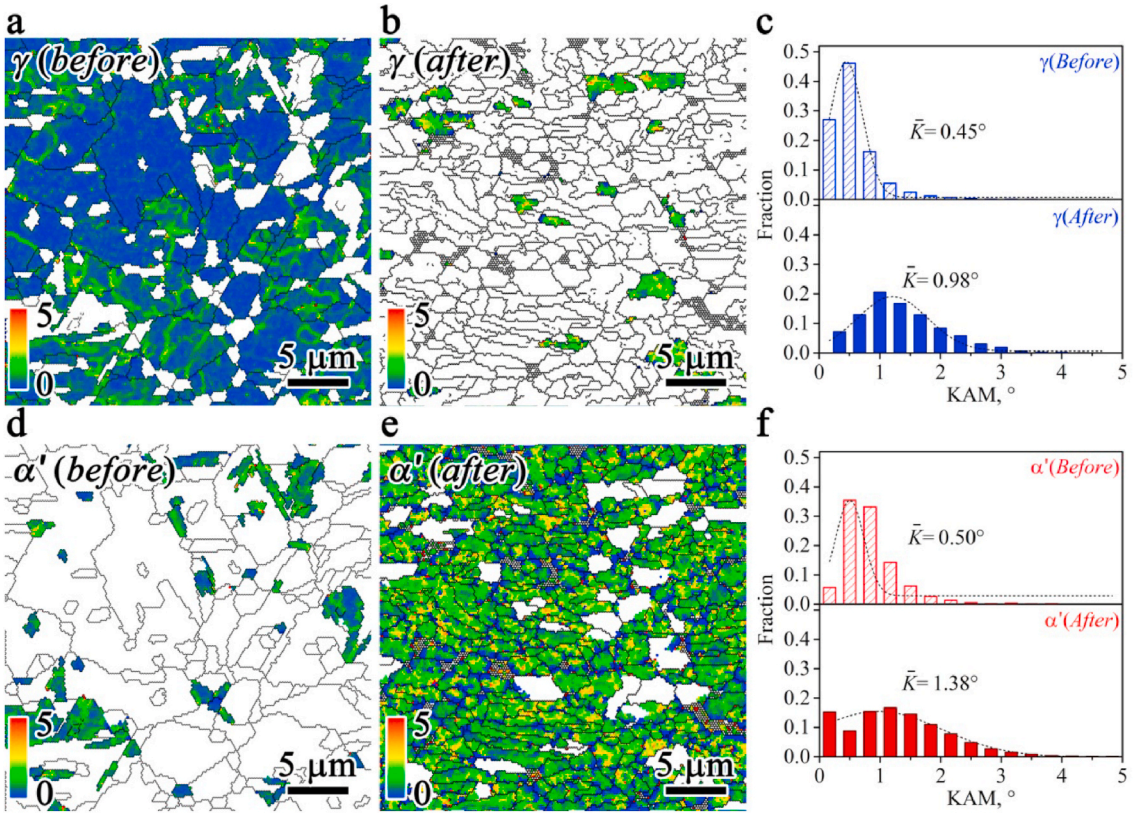

Fig. 9. The maps of KAM values for the aged sample at 550 °C prior to and after tensile testing: (a) (b) for the austenite phase; (d) (e) for the martensite phase. The corresponding statistical distributions of KAM values: (c) for the austenite phase; (f) for the martensite phase.

phenomenon for unloading yield points has also been found in many metals and alloys due to the pile-ups of dislocations during unloading, or the uncoordinated deformation in hetero-materials [53–55]. In FeNiAlC alloy, the B2 precipitates and the transformed martensite both lead to an increased yield stress. The close-up views of typical hysteresis loops for the aged sample at 750 °C are displayed in Fig. 5b. It is shown that the hysteresis loop becomes larger and larger with increasing applied tensile strain, indicating strong HDI hardening. Here, the HDI stress (σ_{HDI}) was calculated using the method proposed in our previous paper [41]. The reverse plastic strain (ε_{rp}), i.e., the width of the hysteresis loop as defined in Fig. 5b, can also considered as an indicator of the HDI hardening. Both σ_{HDI} and ε_{rp} are plotted as a function of the applied true tensile strain in Fig. 5c, and the results indicate that all samples show strong HDI hardening due to the interactions between various phases with different mechanical properties. The fraction of the HDI stress in the total flow stress ($\sigma_{HDI}/\sigma_{total}$) can be considered as the contribution of back stress hardening to the overall strain hardening, thus the evolutions of $\sigma_{HDI}/\sigma_{total}$ along with applied tensile true strain for various samples are displayed in Fig. 5d. It is interesting to note that $\sigma_{HDI}/\sigma_{total}$ for the aged samples is higher than that for the HR sample, and the aged sample at 550 °C has the highest $\sigma_{HDI}/\sigma_{total}$. These observations indicate that the aged samples have higher HDI hardening, and the aged sample at 550 °C has the highest HDI hardening. The higher HDI hardening for the aged samples results in better strain hardening ability under tensile loading,

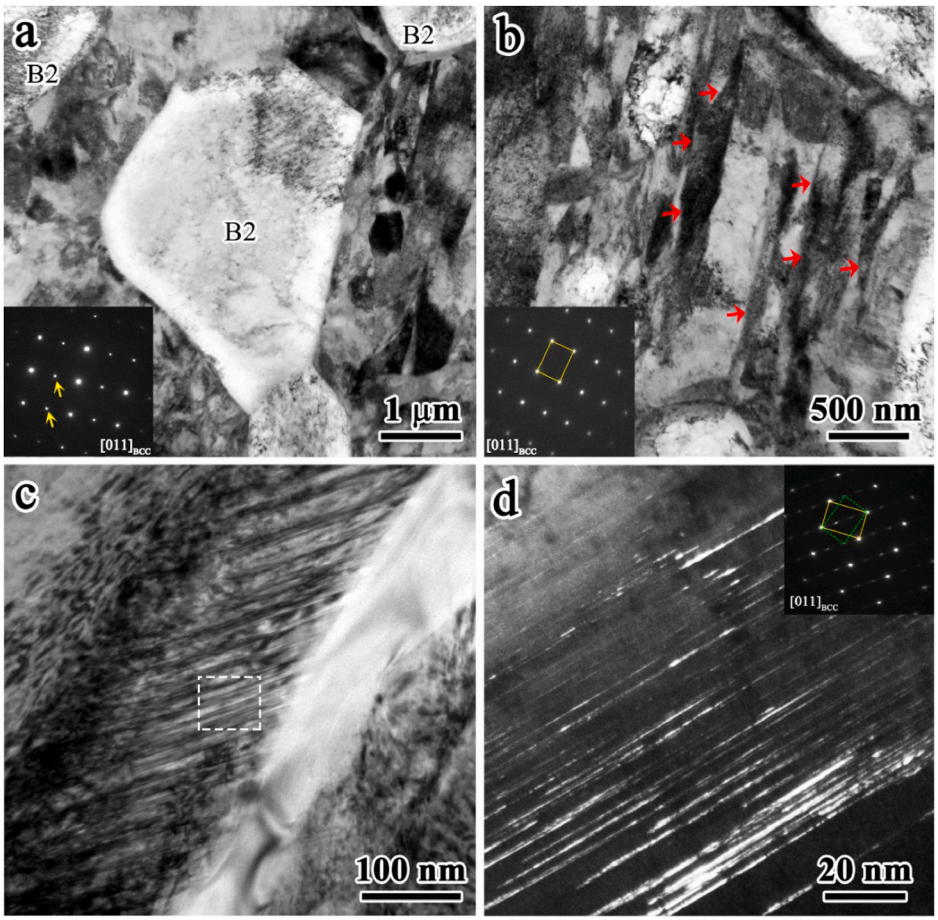

Fig. 10. TEM images after deformation for the aged sample at 550 °C. (a) B2 grain with low dislocation density. (b) Deformation-induced lath martensite with high dislocation density. (c) Martensite grains with high density of twins. (d) The dark field close-up view for the rectangular area in (c).

as indicated in Fig. 4a.

In order to reveal the amount of the martensite transformation during the tensile deformation, the XRD diffraction patterns in the HR sample and in the aged sample at 550 °C prior to and after tensile deformation have been obtained. Then, the volume fraction of γ austenite phase can be estimated by the methods mentioned previously. The information for the volume fractions of γ austenite phase before and after tensile deformation and the amounts of phase transformation during tensile tests for the two samples are provided in Fig. 6. The XRD data reveal significant phase transformation during tensile tests for both samples. As indicated, the volume fractions of the austenite phase are much smaller after tensile deformation for the aged sample compared to that for the HR sample, which indicates that the stability of the austenite phase upon deformation is much reduced for the aged sample. It is also shown that the amount of phase transformation during tensile testing is much larger for the aged sample at 550 °C, which is consistent with the strongest HDI hardening as shown in Fig. 5d. This reduced stability of the austenite phase for the aged sample might be attributed to two reasons: (i) the high local stress level induced by the undeformable and hard B2 precipitates around the austenite grains [33–36], and these induced high local stresses should promote the martensite transformation; (ii) diffusion of nickel and aluminum from the austenite phase to the B2 precipitates during aging, and poverty of nickel in the austenite phase for the aged sample should also facilitate the martensite transformation [56,57]. The promoted martensite transformation should result in stronger strain hardening as shown in Fig. 5c and d.

The EBSD phase images with GBs (the same color coding is used as Fig. 1a–d) for various samples after tensile tests are shown in Fig. 7a–d. It is shown that the volume fraction of γ austenite phase is much reduced after tensile tests for all samples, indicating phase transformation. Based on EBSD observations, it is also shown that volume fractions of the austenite phase are much smaller after tensile deformation for the aged samples compared to that for the HR sample, which is consistent with the XRD results in Fig. 6. Based on the EBSD images prior to and after tensile tests for various samples, the grain size changes of three phases for various samples can be obtained.

The estimated average grain sizes of austenite grains, martensite grains and B2 precipitates after tensile testing for the HR sample and the aged samples are displayed in Fig. 8a, while the average size reductions of austenite grains, martensite grains and B2 precipitates after tensile testing for various samples are displayed in Fig. 8b. The grain refinement of austenite grains can be attributed to the significant phase transformation from austenite phase to martensite phase during tensile loading and the nucleation of martensite grains inside the austenite grains. It can also be seen that the size reduction of austenite grains is largest for the sample aged at 550 °C due to the highest amount martensite transformation during tensile deformation. The grain refinement of martensite grains during tensile deformation can be attributed to the formed small size lath martensite during tensile loading. These formed lath martensite with small size should have strong impact on the strain hardening behavior. The size change for the B2 precipitates is not obvious during tensile deformation.

The kernel average misorientation (KAM) values of various phases for the aged sample at 550 °C prior to and after tensile testing are displayed in Fig. 9. The KAM maps for the austenite phase are shown in Fig. 9a and b, while the KAM distributions for the martensite phase are displayed in Fig. 9d and e. The corresponding statistical distributions of KAM values are shown in Fig. 9c and f. In general, the KAM values can

reflect the density of geometrically necessary dislocations (GNDs) [19, 20]. It can be observed that the dislocation density is relatively low in austenite grains before tensile testing due to the aging treatment. The change of KAM values for austenite grains can be ignored since the volume fraction of the austenite phase is very small after tensile deformation. However, the KAM values become much larger after tensile testing for the martensite phase. This indicates that the dislocation density in martensite phase increases significantly during the phase transformation, which can be attributed to the generation of transformation-induced dislocations during tensile deformation [58]. These transformation-induced dislocations can also have great impact on the strain hardening.

The TEM images for the aged sample at 550 °C after tensile testing are shown in Fig. 10. As indicated in Fig. 10a, the dislocation density is very low in the B2 grains and very few substructures (dislocation wall, dislocation cell, etc.) can be observed inside the B2 grains after tensile testing. This indicates that the hard B2 grains are nearly undeformable, and the applied tensile strain is mostly accommodated by the other two phases. Deformation-induced lath martensite with high dislocation density can be observed after tensile deformation (Fig. 10b), which indicates that the martensite phase can carry part of strain during tensile loading. Moreover, the density of twins becomes much higher for the martensite grains after tensile deformation (Fig. 10c and d), and these deformation-induced nanotwins should contribute significantly to the strain hardening, as the dynamic Hall-Petch effect for TWIP effect [59]. These deformation-induced TBs should reduce the free path of dislocation glide and provide strong barriers for dislocation slip, resulting in strong strain hardening.

4. Summary and concluding remarks

In the present study, aging and WQ at critical temperatures have been applied to a HR FeNiAlC dual-phase alloy to obtain B2 intermetallic precipitates with various volume fractions and sizes, resulting in a so-called triplex microstructure. The tensile properties have been tested, and the corresponding deformation mechanisms were carefully revealed by LUR tests and microstructure characterizations before and after tensile testing. The main findings can be summarized as follows:

(1) Higher yield strength, higher ratio between the ultimate strength and the yield strength, and stronger strain hardening were achieved in the aged samples compared to these for the HR sample. All samples show strong HDI hardening due to the interactions between various phases with different mechanical properties, the aged samples have higher HDI hardening and the aged sample at 550 °C has the highest HDI hardening.
(2) Compared to that for the HR sample, the stability of the austenite phase upon deformation is much reduced for the aged sample, which can be attributed to the following two reasons: the high local stress level induced by the undeformable and hard B2 precipitates around the austenite grains, and the diffusion of nickel and aluminum from the austenite phase to the B2 precipitates during aging. Thus, the amount of phase transformation during tensile tests is much larger for the aged samples, resulting in stronger strain hardening.
(3) Deformation-induced lath martensite with high dislocation density is observed after tensile deformation, and these transformation-induced dislocations should have significant influence on the strain hardening. Moreover, the tensile deformation also induces nanotwins in the martensite grains, resulting in much higher density of twins and smaller spacing for twins after tensile loading. These deformation-induced TBs with nanoscale should reduce the free path of dislocation glide and provide strong barriers for dislocation slip, resulting in strong strain hardening as the dynamic Hall-Petch effect. The present results should provide insights for tailoring microstructures for achieving better strength-ductility synergy in metals and alloys.

Data availability

The raw/processed data required to reproduce these findings cannot be shared at this time due to technical or time limitations.

CRediT authorship contribution statement

Yan Ma: Investigation, Writing - original draft, preparation. **Lingling Zhou:** Investigation. **Muxin Yang:** Investigation. **Fuping Yuan:** Conceptualization, Writing - original draft, preparation, Supervision. **Xiaolei Wu:** Conceptualization, Supervision.

Declaration of competing interest

The authors declare that they have no known competing financial interests or personal relationships that could have appeared to influence the work reported in this paper.

Acknowledgements

This work was supported by the National Key R&D Program of China [grant number 2017YFA0204402]; the National Natural Science Foundation of China [grant numbers 11672313 and 11572328], and the Strategic Priority Research Program of the Chinese Academy of Sciences [grant numbers XDB22040503].

Appendix A. Supplementary data

Supplementary data to this article can be found online at https://doi.org/10.1016/j.msea.2020.140498.

References

[1] R.Z. Valiev, Nanostructuring of metals by severe plastic deformation for advanced properties, Nat. Mater. 3 (2004) 511–516.
[2] T.G. Langdon, Twenty-five years of ultrafine-grained materials: achieving exceptional properties through grain refinement, Acta Mater. 61 (2013) 7035–7059.
[3] Y.T. Zhu, X.Z. Liao, Nanostructured metals: retaining ductility, Nat. Mater. 3 (2004) 351–352.
[4] X.L. Wu, F.P. Yuan, M.X. Yang, P. Jiang, C.X. Zhang, L. Chen, Y.G. Wei, E. Ma, Nanodomained nickel unite nanocrystal strength with coarse-grain ductility, Sci. Rep. 5 (2015) 11728.
[5] O. Bouaziz, S. Allain, C.P. Scott, P. Cugy, D. Barbier, High manganese austenitic twinning induced plasticity steels: a review of the microstructure properties relationships, Curr. Opin. Solid State Mater. Sci. 15 (2011) 141–168.
[6] J.G. Sevillano, F.D.L. Cuevas, Internal stresses and the mechanism of work hardening in twinning-induced plasticity steels, Scripta Mater. 66 (2012) 978–981.
[7] F.D. Fischer, G. Reisner, E. Werner, K. Tanaka, G. Cailletaud, T. Antretter, A new view on transformation induced plasticity (TRIP), Int. J. Plast. 16 (2000) 723–748.
[8] S. Cheng, X.L. Wang, Z. Feng, B. Clausen, H. Choo, P.K. Liaw, Probing the characteristic deformation behaviors of transformation-induced plasticity steels, Metall. Mater. Trans. 39A (2008) 3105–3112.
[9] L. Lu, X. Chen, X. Huang, K. Lu, Revealing the maximum strength in nanotwinned copper, Science 323 (2009) 607–610.
[10] X.Y. Li, Y.J. Wei, L. Lu, K. Lu, H.J. Gao, Dislocation nucleation governed softening and maximum strength in nano-twinned metals, Nature 464 (2010) 877–880.
[11] T.H. Fang, W.L. Li, N.R. Tao, K. Lu, Revealing extraordinary intrinsic tensile plasticity in gradient nano-grained copper, Science 331 (2011) 1587–1590.
[12] X.L. Wu, P. Jiang, L. Chen, F.P. Yuan, Y.T. Zhu, Extraordinary strain hardening by gradient structure, Proc. Natl. Acad. Sci. U.S.A. 111 (2014) 7197–7201.
[13] Y.M. Wang, M.W. Chen, F.H. Zhou, E. Ma, High tensile ductility in a nanostructured metal, Nature 419 (2002) 912–915.
[14] Y. Ma, F.P. Yuan, M.X. Yang, P. Jiang, E. Ma, X.L. Wu, Dynamic shear deformation of a CrCoNi medium-entropy alloy with heterogeneous grain structures, Acta Mater. 148 (2018) 407–418.
[15] Z.L. Yang, M.X. Yang, Y. Ma, L.L. Zhou, W.Q. Cheng, F.P. Yuan, X.L. Wu, Strain rate dependent shear localization and deformation mechanisms in the CrMnFeCoNi high-entropy alloy with various microstructures, Mater. Sci. Eng. A 793 (2020), 139854.

[16] X.L. Wu, M.X. Yang, F.P. Yuan, G.L. Wu, Y.J. Wei, X.X. Huang, Y.T. Zhu, Heterogeneous lamella structure unites ultrafine-grain strength with coarsegrain ductility, Proc. Natl. Acad. Sci. U.S.A. 112 (2015) 14501–14505.
[17] X.L. Ma, C.X. Huang, J. Moering, M. Ruppert, H.W. Höppel, M. Göken, J. Narayan, Y.T. Zhu, Mechanical properties of copper/bronze laminates: role of interfaces, Acta Mater. 116 (2016) 43–52.
[18] J.Y. He, Y. Ma, D.S. Yan, S.H. Jiao, F.P. Yuan, X.L. Wu, Improving ductility by increasing fraction of interfacial zone in low C steel/304 SS laminates, Mater. Sci. Eng. A 726 (2018) 288–297.
[19] J.Y. He, F.P. Yuan, M.X. Yang, L.L. Zhou, S.H. Jiao, X.L. Wu, Exceptional tensile properties under cryogenic temperature in heterogeneous laminates induced by non-uniform martensite transformation and strain delocalization, Mater. Sci. Eng. A 791 (2020), 139780.
[20] P.V. Liddicoat, X.Z. Liao, Y.H. Zhao, Y.T. Zhu, M.Y. Murashkin, E.J. Lavernia, R. Z. Valiev, S.P. Ringer, Nanostructural hierarchy increases the strength of aluminum alloys, Nat. Commun. 1 (2010) 63.
[21] G. Liu, G.J. Zhang, F. Jiang, X.D. Ding, Y.J. Sun, J. Sun, E. Ma, Nanostructured high-strength molybdenum alloys with unprecedented tensile ductility, Nat. Mater. 12 (2013) 344–350.
[22] C. Haase, L.A. Barrales-Mora, D.A. Molodov, G. Gottstein, Tailoring the mechanical properties of a twinning-induced plasticity steel by retention of deformation twins during heat treatment, Metall. Mater. Trans. 44A (2013) 4445–4449.
[23] G. Frommeyer, U. Brüx, P. Neumann, Supra-ductile and high-strength manganese-TRIP/TWIP steels for high energy absorption purposes, ISIJ Int. 43 (2003) 438–446.
[24] Z.M. Li, K.G. Pradeep, Y. Deng, D. Raabe, C.C. Tasan, Metastable high-entropy dual-phase alloys overcome the strength-ductility trade-off, Nature 534 (2016) 227–230.
[25] Z.M. Li, C.C. Tasan, K.G. Pradeep, D. Raabe, A TRIP-assisted dual-phase high-entropy alloy: grain size and phase fraction effects on deformation behavior, Acta Mater. 131 (2017) 323–335.
[26] H. Lee, M.C. Jo, S.S. Sohn, A. Zargaran, J.H. Ryu, N.J. Kim, S. Lee, Novel medium-Mn (austenite + martensite) duplex hot-rolled steel achieving 1.6 GPa strength with 20 % ductility by Mn-segregation-induced TRIP mechanism, Acta Mater. 147 (2018) 247–260.
[27] R. Ding, Z.B. Dai, M.X. Huang, Z.G. Yang, C. Zhang, H. Chen, Effect of pre-existed austenite on austenite reversion and mechanical behavior of an Fe-0.2C-8Mn-2Al medium Mn steel, Acta Mater. 147 (2018) 59–69.
[28] S. Takaki, H. Nakatsu, Y. Tokunaga, Effects of austenite grain-size on ε martensitic transformation in Fe-15mass%Mn alloy, Mater. Trans. 34 (1993) 489–495.
[29] C.W. Sinclair, W.J. Poole, Y. Bréchet, A model for the grain size dependent work hardening of copper, Scripta Mater. 55 (2006) 739–742.
[30] F.P. Yuan, X.D. Bian, P. Jiang, M.X. Yang, X.L. Wu, Dynamic shear response and evolution mechanisms of adiabatic shear band in an ultrafine-grained austenite-ferrite duplex steel, Mech. Mater. 89 (2015) 47–58.
[31] S. Prüger, A. Seupel, M. Kuna, A thermomechanically coupled material model for TRIP-steel, Int. J. Plast. 55 (2014) 182–197.
[32] R. Zaera, J.A. Rodríguez-Martínez, G. Vadillo, J. Fernández-Sáez, Dynamic necking in materials with strain induced martensitic transformation, J. Mech. Phys. Solid. 64 (2014) 316–337.
[33] D. Choudhuri, B. Gwalani, S. Gorsse, M. Komarasamy, S.A. Mantri, S.G. Srinivasan, R.S. Mishra, R. Banerjee, Enhancing strength and strain hardenability via deformation twinning in fcc-based high entropy alloys reinforced with intermetallic compounds, Acta Mater. 165 (2019) 420–430.
[34] I. Gutierrez-Urrutia, D. Raabe, Influence of Al content and precipitation state on the mechanical behavior of austenitic high-Mn low-density steels, Scripta Mater. 68 (2013) 343–347.
[35] Z.Q. Wu, H. Ding, X.H. An, D. Han, X.Z. Liao, Influence of Al content on the strain-hardening behavior of aged low density Fe-Mn-Al-C steels with high Al content, Mater, Sci. Eng. A 639 (2015) 187–191.
[36] J.H. Hwang, T.T.T. Trang, O. Lee, G. Park, A. Zargaran, N.J. Kim, Improvement of strength - ductility balance of B2-strengthened lightweight steel, Acta Mater. 191 (2020) 1–12.
[37] Y. Ma, M.X. Yang, P. Jiang, F.P. Yuan, X.L. Wu, Plastic deformation mechanisms in a severely deformed Fe-Ni-Al-C alloy with superior tensile properties, Sci. Rep. 7 (2017) 15619.
[38] T. Furuta, S. Kuramoto, T. Ohsuna, K. Oh-ishi, K. Horibuchi, Die-hard plastic deformation behavior in an ultrahigh-strength Fe-Ni-Al-C alloy, Scripta Mater. 101 (2015) 87–90.
[39] K. Edalati, T. Furuta, T. Daio, S. Kuramoto, Z. Horita, High strength and high uniform ductility in a severely deformed iron alloy by lattice softening and multimodal-structure formation, Mater. Res. Lett. 3 (2015) 197–202.
[40] M.X. Yang, F.P. Yuan, Q.G. Xie, Y.D. Wang, E. Ma, X.L. Wu, Strain hardening in Fe-16Mn-10Al-0.86C-5Ni high specific strength steel, Acta Mater. 109 (2016) 213–222.
[41] M.X. Yang, Y. Pan, F.P. Yuan, Y.T. Zhu, X.L. Wu, Back stress strengthening and strain hardening in gradient structure, Mater. Res. Lett. 4 (2016) 145–151.
[42] C. Jatczak, Retained Austenite and its Measurement by X-Ray Diffraction, SAE Technical Paper, 1980.
[43] L. Liu, Q. Yu, Z. Wang, J. Ell, M.X. Huang, R.O. Ritchie, Making ultrastrong steel tough by grain-boundary delamination, Science 368 (2020) 1347–1352.
[44] H.S. Wang, J. Kang, W. X Dou, Y.X. Zhang, G. Yuan, G.M. Cao, R.D.K. Misra, G. D. Wang, Microstructure and mechanical properties of hot-rolled and heat-treated TRIP steel with direct quenching process, Mater. Sci. Eng. A 702 (2017) 350–359.
[45] S. Lee, S.J. Lee, S.S. Kumar, K. Lee, B.C. De Cooman, Localized deformation in multiphase, ultra-fine-grained 6 Pct Mn transformation-induced plasticity steel, Metall. Mater. Trans. 42 (2011) 3638–3651.
[46] F. Yang, H.W. Luo, E.X. Pu, S.L. Zhang, H. Dong, On the characteristics of Portevin-Le Chatelier bands in cold-rolled 7Mn steel showing transformation-induced plasticity, Int. J. Plast. 103 (2018) 188–202.
[47] Y.F. Shen, N. Jia, R.D.K. Misra, L. Zuo, Softening behavior by excessive twinning and adiabatic heating at high strain rate in a Fe-20Mn-0.6C TWIP steel, Acta Mater. 103 (2016) 229–242.
[48] X.D. Bian, F.P. Yuan, X.L. Wu, Correlation between strain rate sensitivity and characteristics of Portevin-Le Châtelier bands in a twinning-induced plasticity steel, Mater. Sci. Eng. A 696 (2017) 220–227.
[49] F.K. Yan, G.Z. Liu, N.R. Tao, K. Lu, Strength and ductility of 316L austenitic stainless steel strengthened by nano-scale twin bundles, Acta Mater. 60 (2012) 1059–1071.
[50] C. García-Mateo, F.G. Caballero, The role of retained austenite on tensile properties of steels with bainitic microstructures, Mater. Trans. 46 (2005) 1839–1846.
[51] S.H. Jiang, H. Wang, Y. Wu, X.J. Liu, H.H. Chen, M.J. Yao, B. Gault, D. Ponge, D. Raabe, A. Hirata, M.W. Chen, Y.D. Wang, Z.P. Lu, Ultrastrong steel via minimal lattice misfit and high-density nanoprecipitation, Nature 544 (2017) 460–464.
[52] Y.T. Zhu, X.L. Wu, Perspective on hetero-deformation induced (HDI) hardening and back stress, Mater. Res. Lett. 7 (2019) 393–398.
[53] H.K. Birnbaum, Unloading effects in crystals, Acta Metall. 9 (1961) 320–326.
[54] G. Hawkins, J.T. Evans, Unloading yield-point in 9-percent Ni steel, Scripta Metall. 19 (1985) 1323–1326.
[55] M.J. Makin, Unloading effects in the plastic properties of copper single crystals, Philos. Mag. A 3 (1958) 287–301.
[56] E. De Moor, D.K. Matlock, J.G. Speer, M.J. Merwin, Austenite stabilization through manganese enrichment, Scripta Mater. 64 (2011) 185–188.
[57] Y.H. Yang, Q.W. Cai, D. Tang, H.B. Wu, Precipitation and stability of reversed austenite in 9Ni steel, Int. J. Miner. Metall. Mater. 17 (2010) 587–595.
[58] B.B. He, B. Hu, H.W. Yen, G.J. Cheng, Z.K. Wang, H.W. Luo, M.X. Huang, High dislocation density-induced large ductility in deformed and partitioned steels, Science 357 (2017) 1029–1032.
[59] I. Gutierrez-Urrutia, D. Raabe, Grain size effect on strain hardening in twinning-induced plasticity steels, Scripta Mater. 66 (2012) 992–996.